ORIGINAL ARTICLE

Effects of preheating on laser beam–welded NSSC 2120 lean duplex steel

Michał Landowski[1] · Soma Csaba Simon[2] · Csaba Breznay[2] · Dariusz Fydrych[1] · Balázs Varbai[2]

Abstract

Duplex stainless steels show sustainable alternative for the conventional austenitic grades, with higher strength, higher resistance against stress corrosion cracking, and lower purchase cost. Thus, duplex stainless steel gains more attention in construction, oil and gas, and chemical industries. Among duplex stainless steels, low nickel and low molybdenum alloyed lean duplex stainless steel are a cost-effective substitution of austenitic grades. However, keeping the balanced ferrite/austenite phase ratio in the weld metal can be challenging, mostly for autogenous and low heat input welding processes. In our research, a newly developed NSSC 2120 lean duplex stainless steel grade was welded autogenously by fiber laser welding process. Different welding parameters and preheating temperatures were used during the experiments. The welds were evaluated by microscopic and metallographic techniques, and also by electrochemical corrosion measurements. The welding parameters and the preheating temperature greatly influenced the weld shape and the austenite content in the weld metal. It was found that the focus point distance from the sheet surface had significant effect on the weld geometry. Changing the focus point distance to $+2$ mm, the penetration depth increased from 4.96 to 5.53 mm, and increased the austenite content by 2.6%. Due to the preheating the welds became wider and shallower, e.g., from 4.96 to 4.08 mm penetration depth, while the cross-section are increased from 5.10 to 6.12 mm^2 at the same sample. The preheating resulted in more intergranular austenite formation, which meant maximum 4% increase in the weld metal. The increasing austenite content resulted in increasing pitting corrosion resistance in 3.5% NaCl electrolyte, the highest increase was 90 mV.

Keywords Lean duplex steel · Laser beam welding · Preheating · Weld geometry · Pitting corrosion resistance

1 Introduction

Among the family of stainless steels duplex stainless steels (DSS) show a high strength alternative compared to the conventional austenitic grades, with better resistance against certain corrosion mechanisms, such as stress corrosion cracking [1–4]. DSSs have usually higher chromium (Cr) and lower nickel (Ni) alloying than the austenitic grades. The specific alloying content and the annealing heat treatment results in a double, ferritic-austenitic microstructure in all DSS grades, with the ferrite content around 40%.

DSSs can be classified according to their alloying content, and the governing corrosion resistance. The lean duplex stainless steels (LDSS) are low Ni and molybdenum (Mo) alloyed. LDSSs showing a great alternative to substitute conventional, Mo-free austenitic grades (like AISI 304). The approximately double yield strength and lower price (due to the lower Ni and Mo content) making LDSSs a cost-effective and sustainable solution in chemical, civil, constructional, and oil and gas industries [5–9]. In LDSS grades the austenite promoting, and corrosion resistance effect of Ni is substituted with higher manganese (Mn), nitrogen (N), and sometimes copper (Cu) additions [10–13].

In the weld metal (WM) and in the heat affected zone (HAZ) of duplex grades, the phase balance is usually shifted to the more ferritic microstructures. The reason for this is the relatively fast cooling rate during conventional welding processes (mostly in the HAZ). As all duplex

✉ Balázs Varbai
varbai.balazs@gpk.bme.hu

1 Institute of Manufacturing and Materials Technology, Faculty of Mechanical Engineering and Ship Technology, Gdańsk University of Technology, Gabriela Narutowicza Street 11/12, 80-233 Gdańsk, Poland

2 Budapest University of Technology and Economics, Műegyetem Rkp. 3, 1111 Budapest, Hungary

grades solidify as ferrite, the balanced microstructure of all DSS and LDSS grades is a result of solid-state phase transformation from ferrite to austenite. This phase transformation is mainly driven by the nitrogen diffusion in the ferritic microstructure, as N is a potent austenite forming element, and has a high diffusion rate in ferrite [14–19]. Slow cooling rates are also detrimental, as they promote ferrite decomposition into harmful intermetallic precipitations, which deteriorate corrosion resistance and toughness [20–23]. Thus, the recommended heat input for DSS and LDSS welding is limited from both below and above.

With conventional arc welding processes and additional filler materials the phase balance can usually be kept at an adequate level (neither the ferrite nor the austenite content is higher than 70%). However, high energy density welding processes such as laser beam welding (LBW) or electron beam welding (EBW) challenges welding researchers. The high energy density during these welding processes result in very rapid cooling rates (short cooling times), thus the ferrite to austenite phase transformation is suppressed [24–29]. Researchers try different techniques to promote austenite formation in the LBW and EBW welds. One solution is to use Ni-rich filler materials [30, 31]. The Ni promotes austenite formation during the solidification process and the subsequent austenite formation. Using nitrogen as a shielding gas also promotes austenite formation in the weld metal [32–34]. If the welding process cannot be modified, preheating or post weld heat treatment (PWHT) can be used. Generally, neither preheating nor post weld heat treatment is recommended in the case of DSS welding, as the slower cooling rate can promote intermetallic formation. Schmigalla et al. [35] found that the preheating temperature decreased the ferrite content in the weld metal in the case of EBW of different duplex grades. However, this ferrite content decrease is only 6% between 200 and 400 °C preheating temperatures. Krasnorutskyi et al. [36] also used different preheating temperatures during the EBW of grade GX2CrNiMoN22-5–3 to slow down cooling rate after welding. Their results showed that the highest preheating temperature (435 °C) resulted in the lowest ferrite content, which was still around 70%. Kolenič et al. [37] used defocused electron beam to preheat and post heat the EBW welds of 2507 super duplex grade. They found that, with the additional heat input the ferrite/austenite balance can be controlled. On the other hand, the additional heat treatment had only minor effects on the corrosion resistance. PWHT is also sometimes used in order to promote austenite formation in the HAZ and WM. Saravanan et al. [38] used 1050 °C PWHT for 2 h to improve the corrosion resistance of LBW super duplex stainless steel 2507 through reducing ferrite content and promoting austenite transformation. They found that PWHT increased austenite formation with secondary austenite precipitation in the

ferrite grains. Köse et al. [39] showed the same secondary austenite formation in the ferrite grains after PWHT.

To make duplex stainless steels able for higher heat input welding processes such as submerged arc welding, and to suppress intermetallic formation during longer cooling times, steel manufacturers made efforts to develop new types of grades. Grade 2120, developed by Nippon Steel Stainless Steel Corporation (NSSC), is one of the new lean duplex grades, which can keep a stable phase balance at lower cooling rates. The newly developed 2120 grade has double the strength compared to AISI 304, while maintaining better corrosion resistance. The intermetallic formation is also suppressed in the HAZ and WM, making this grade able to be welded as high heat inputs as 3.5 kJ/mm, while conventional duplex grades are recommended to be welded with maximum 2.5 kJ/mm heat input [40]. These features make this grade excellent for constructional applications, showing a cost-effective and sustainable solution.

In our research, we performed autogenous fiber laser beam welding on NSSC 2120 lean duplex stainless steel with different welding parameters, using room temperature, and 300 °C preheating, as the service temperature limit for different duplex grades is usually around this temperature, e.g., 315 °C according to ASME Code Div. 1—part II. The welds were evaluated by microstructural characterization and electrochemical corrosion tests.

2 Materials and methods

2.1 Base material

For the laser welding experiments, a newly developed NSSC 2120 type lean duplex stainless steel sheets have been used with the thickness of 6 mm. The NSSC 2120 LDSS has been developed to be applicable for high heat input welding (such as submerged arc welding) in order to reduce welding passes. The precipitation behavior of 2120 has been suppressed with special alloying and steel manufacturing techniques. The grade 2120 is mainly used in constructional and civil industries, in thicker wall thicknesses, mostly to substitute conventional austenitic grade 304. The chemical composition of the base material 2120 can be seen in Table 1, according to the manufacturer's datasheet. The high strength (~ 500 MPa 0.2% proof stress) and the duplex austenitic ferritic microstructure is provided with higher Mn, N, and Cu alloying, comparing to the conventional duplex grades. With the N addition the austenite formation is promoted in the HAZ, which reduces the Cr_2N formation to a starting temperature of 910 °C [40]. The Cr_2N precipitation would lead to a loss of pitting corrosion resistance, and thus it is important to suppress its formation in the highly ferritic HAZ, by the promotion of austenite formation, which has

much higher solubility of N. Thus, the manufacturer also aimed to have maximum 50% ferrite in the base metal in the annealed state [40].

2.2 Welding parameters

To ensure constant welding parameters FANUC M710iC/70 type welding robot has been used during the laser welding experiments. The welding robot was equipped with IPG YLS-6000 ytterbium fiber laser welding source. For shielding gas argon in 5.0 purity was used. To investigate the effects of welding parameters to the weld metal shape, microstructure, and corrosion resistance, bead-on-plate welds were made. The sheets were cleaned with acetone and were fixed in a welding table fixture prior to the welding. The welding parameters can be seen in Table 2. From each set of experiments three samples were examined. The welding setup can be seen in Fig. 1.

During the parameter optimization our aim was to have the deepest penetration, which can be achieved by this laser power source. At first, we set the laser power to the possible maximum (which is 6.0 kW) and selected the travel speed, which results in the best geometrical appearance of the weld according to ISO 13919–1. For the highest laser power, the optimal travel speed was selected as 50 mm/s (sample #1). At second, we investigated the effects of the

Table 1 The chemical composition of the base material NSSC 2120 lean duplex grade, according to the manufacturer's datasheet

C	Si	Mn	P	S	Ni	Cr	Mo	Cu	N
0.019	0.38	3.0	0.024	0.001	2.03	20.9	0.28	1.08	0.18

Table 2 The welding parameters used for the laser welding experiments of NSSC 2120 grade

Sample no	Laser beam power (kW)	Laser beam travel speed (mm/s)	Focus point distance (mm)	Shielding gas type and flow rate (l/min)	Preheating temperature (°C)
#1	6.0	50	0	Ar 5.0, 20	RT/300
#2	3.0	25	0	Ar 5.0, 20	RT/300
#3	4.5	37	0	Ar 5.0, 20	RT/300
#4	6.0	50	-2	Ar 5.0, 20	RT/300
#5	6.0	50	2	Ar 5.0, 20	RT/300

Fig. 1 The setup of the fiber laser welding experiments
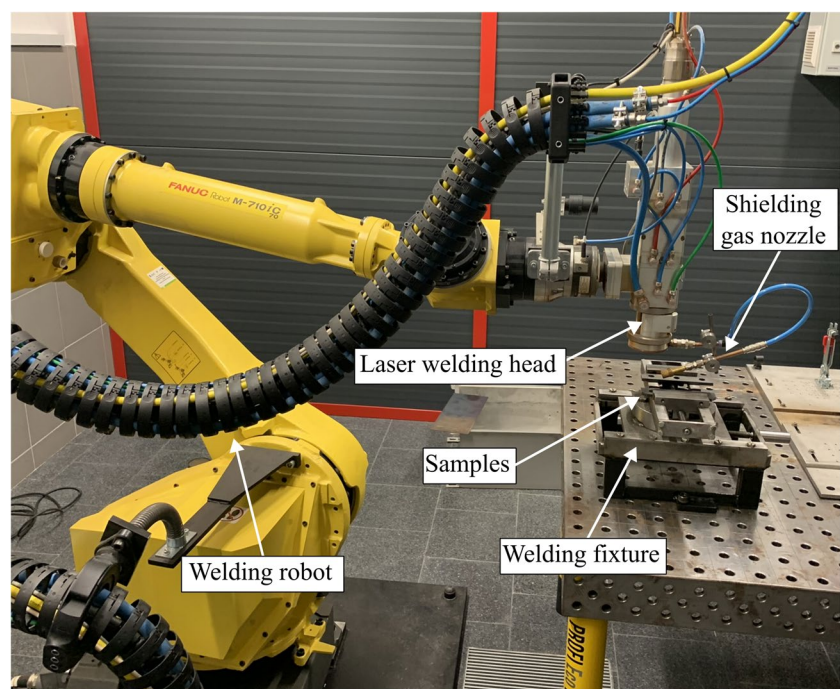
travel speed and the laser power, while keeping the nominal heat input (ratio between the laser power and travel speed) constant. So, for 3.0 kW laser power half of the travel speed, 25 mm/s (sample #2), and for 4.5 kW, 37 mm/s (sample #3) was selected. In the third step, we investigated the effects of the focus point distance. We selected the highest laser power set of parameters to modify the focus point distance from − 2 to + 2 mm, measure from the surface of the sheets (samples #4 and #5) to see the expected most significant differences. The nominal heat input was kept approximately constant in all cases. The focal length of the laser head was 250 mm, and the beam diameter at the focus was about 0.35 mm. To investigate the weld metal and heat affected zone microstructure to lower cooling rates (longer cooling times, which promotes precipitate formation), different preheating temperatures were used. For the laser welding experiments, no welding consumable or backing gas has been used. All the 5 samples were welded at room temperature (RT), and preheated to 300 °C. Accordingly, the samples are marked as #1/RT, #1/300, etc. in the following. The sample preheating was done in an iZO type resistance heater electric furnace, where the temperature distribution in the chamber was assured by fan thermal circulation. After the peak temperature was reached the samples were held in the furnace for 60 min. After taken out, the samples were immediately set in the fixture for welding. The temperature was verified by a contact thermometer prior to the welding.

2.3 Microstructure evaluation

To investigate the weld shape, microstructure, and corrosion resistance of the welded samples, standard metallographic samples were made for the cross section of the welds. The location of the samples was selected from the uniform weld bead sections. The samples were cut by a metallographic cutter under constant cooling. The cut samples then were mounted in epoxy resin and grinded to 4000 grit paper, followed by polishing with 3 µm diamond suspension. To reveal and examine the microstructure, color etching technique was used. With Beraha's tint etchant (60 ml H_2O + 30 ml HCl + 0.75 g $K_2S_2O_5$), the austenite-to-ferrite phase ratio was measured after 15 s of etching time. The austenite content in the weld metal was measured by an image analyzing technique, described in [41]. The weld shape was measured by an Olympus SZX16 stereomicroscope, and the microstructure was examined by an Olympus PMG3 light optical microscope.

2.4 Electrochemical corrosion testing

To investigate the corrosion resistance of the laser beam–welded samples, electrochemical corrosion tests were conducted in a standard three electrode cell. The reference electrode was saturated Ag/AgCl, the counter electrode was a Pt mesh, and the working electrode was the mounted sample. The samples were grinded with 600 grit paper prior to the testing and immersed immediately to the electrolyte. To prevent crevice corrosion during the tests, the samples were covered in polyacrylate resin before the mounting. The electrolyte was 3.5 wt% NaCl, de-aerated with 1 h argon purging prior to the test. The pH value of the electrolyte before the tests was 6.0. The tests were performed at room temperature. The scanning rate during the polarization tests was 1 mV/s, after a 1-h immersion time. As a characteristic property of the corrosion resistance, the corrosion potential (E_{corr}) and the pitting potential (E_{pit}) were selected. The E_{corr} can be measured from the polarization curves, where the cathodic (reduction) and anodic (oxidation) sections intersect. The E_{pit} value shows the stable pitting formation, represented in sharp and steady increase in the corrosion current (i). The E_{pit} values were determined graphically from the polarization curves. The exposed surfaces to the electrolyte were 1 cm^2 in all cases.

3 Results and discussion

3.1 Macroscopic examination of the laser beam–welded samples

The as-welded state of the samples can be seen in Fig. 2. All of the welding parameters can be successfully used to weld NSSC 2120 lean duplex plates; however, there are significant differences in-between the weld geometries. All of the faces of welds are uniform, which shows stable laser beam welding process. Comparing the preheated and non-preheated (RT) samples, it can be seen in Fig. 2. The weld bead width increased due to preheating. On the other hand, the penetration depth seems to decrease as a result of 300 °C preheating temperature. In the case of the samples welded initially at room temperature sample #5 showed full penetration, samples #1 and #3 melting through, and samples #1, #2, and #4 had practically no weld root. Comparing these results to the welding parameters listed in Table 1, it can be seen that laser beam power, travel speed, and the focus point distance altogether have effect on the weld geometry on the contrary to that all of the welds were made with the same theoretical heat input. Comparing samples #1, #4, and #5 to each other (where only the focus point distance changed), it can be seen the higher focus points resulted in deeper penetration. In the case of sample #4 the focus point distance was − 2 mm, which resulted in practically no weld root, in the case of sample #1, it was 0 mm, which showed partial melt through, and in the case of #5 the + 2 mm focus distance resulted in full penetration, with uniform weld root. When the samples were preheated to 300 °C, the penetration

Fig. 2 The face and the root sides of the non-preheated and preheated samples in as-welded condition
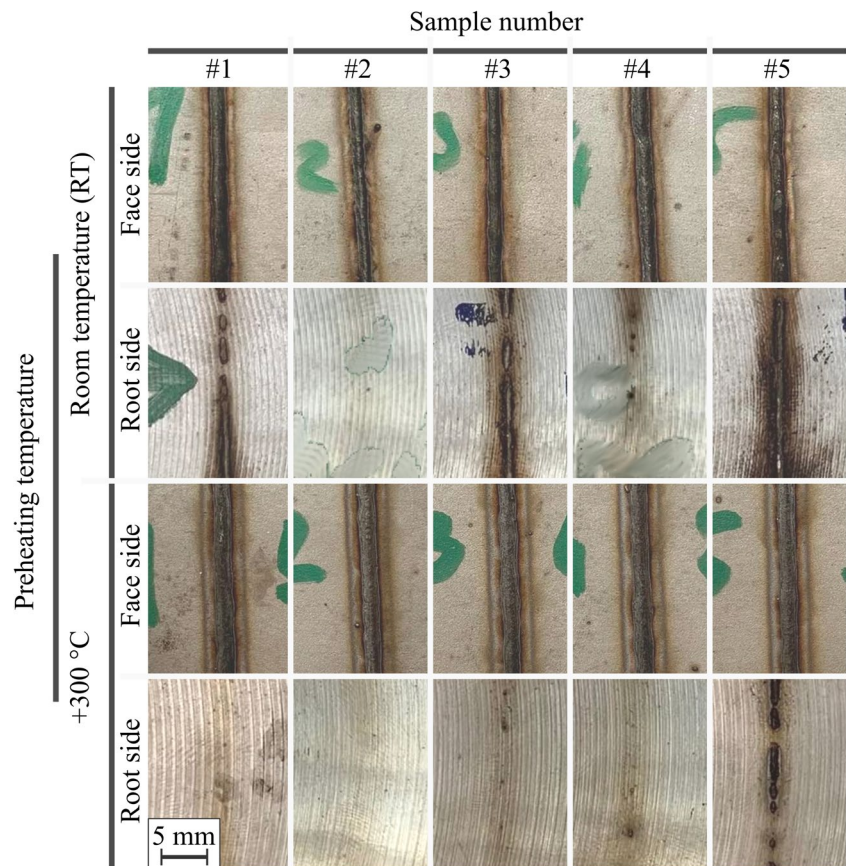
depth significantly decreased, while the weld bead width increased. In the case of the preheated samples, only sample #5 showed partial melt through, while all of the other samples had no weld root. The reason for this is the difference in the temperature gradient next to the heat source. When the samples are not preheated, the temperature gradient is steeper, which results in narrower and deeper welds, on the contrary to the preheated samples, where are visibly wider, but shallower welds.

3.2 Weld shape and geometry

The cross-section of the welds can be seen in Fig. 3. It is evident, that both the welding parameters and the initial temperature have significant effect on the weld shape. Comparing samples #1/RT and #2/RT, the lower travel speed resulted in a narrower weld bottom, while the penetration depth and the weld bead width practically did not change. When the laser power and the travel speed was set in-between the parameters #1 and #2, the penetration deepened, and the bead width became narrower, as it can be seen in the case of sample #3/RT. Modifying the focus point distance also has a notable influence on the weld geometry. Both samples #4/RT and #5/RT showing deeper penetration compared to sample #1/RT. The bottom side of

the sample #4/RT not evenly following the weld geometry, which resulted in the partial melt through as it can be seen in Fig. 2. Sample #5/RT shows even weld shape even at the bottom side, which resulted in the complete and uniform penetration. Preheating the sheets to 300 °C prior to welding has a significant effect on the weld shape. With preheating the temperature gradient has changed around the fusion zone, which results in slower cooling rates, and longer cooling times. Also, the laser beam absorption is increasing with the temperature [42, 43]. Su et al. [44] showed that the preheating is increasing the laser absorption capacity of medium alloyed structural carbon steels, which lead to an increase in the weld bead width. In our research, we confirmed that, the preheated welded samples showing wider but shallower weld geometries in all cases. It also can be seen, due to the different temperature gradient, the welded cross-section became larger in the case of the preheated samples. Comparing samples #2/RT and #2/300, and #3/RT and #3/300, the penetration depth greatly decreased, while the bead width the cross-section area increased. This phenomenon is not that significant at the rest of the welding parameters, although all of the welds showing shallower penetration. This effect in the change of the weld geometry can be helpful in improving the gap tolerance in LBW of butt-welds, as penetration

Fig. 3 The cross-sections of the laser beam–welded samples, welded with different parameters and different preheating temperatures
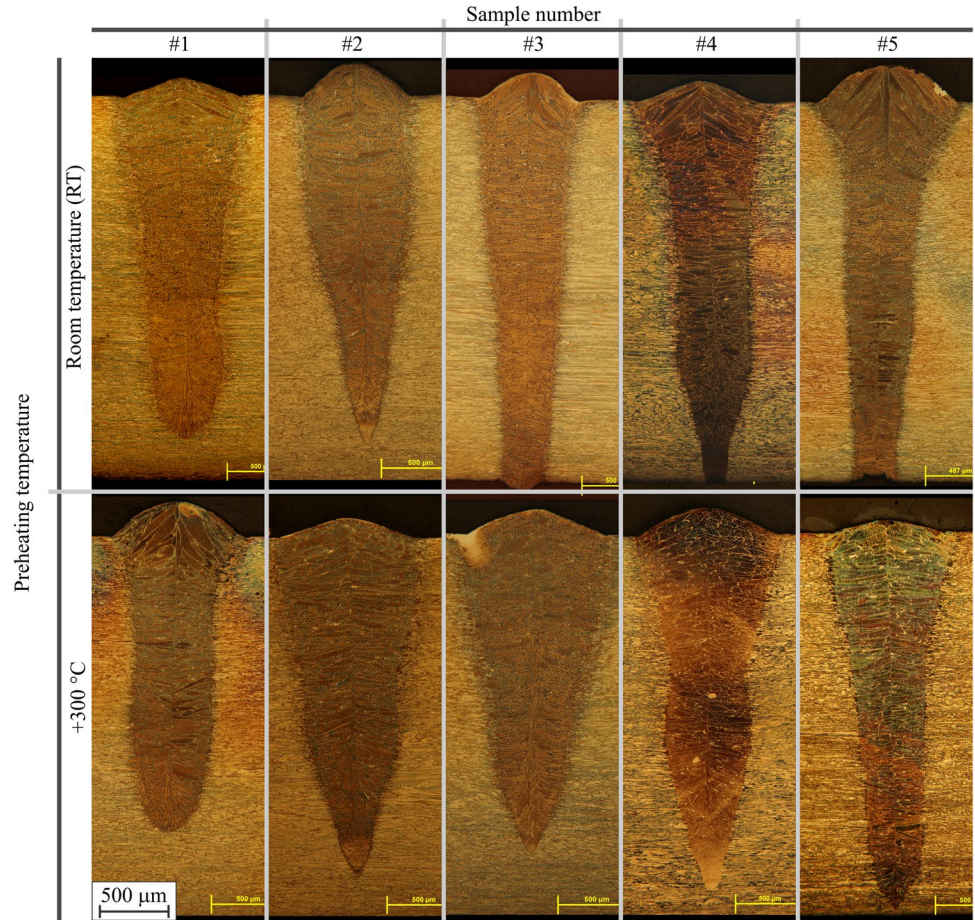

depth is highly sensitive to the air gap in-between the plates in the case of LBW.

The comparison of the weld bead widths can be seen in Fig. 4. The error bars show standard deviation in all graphs.

Reviewing the RT samples, the welding parameters have the most significant effect on the bead width. Comparing samples #1/RT, #4/RT, and #5/RT, where only the focus point distance changed, the bead width is practically the same;

Fig. 4 The weld bead width of the laser beam–welded samples, welded with different parameters and different preheating temperatures
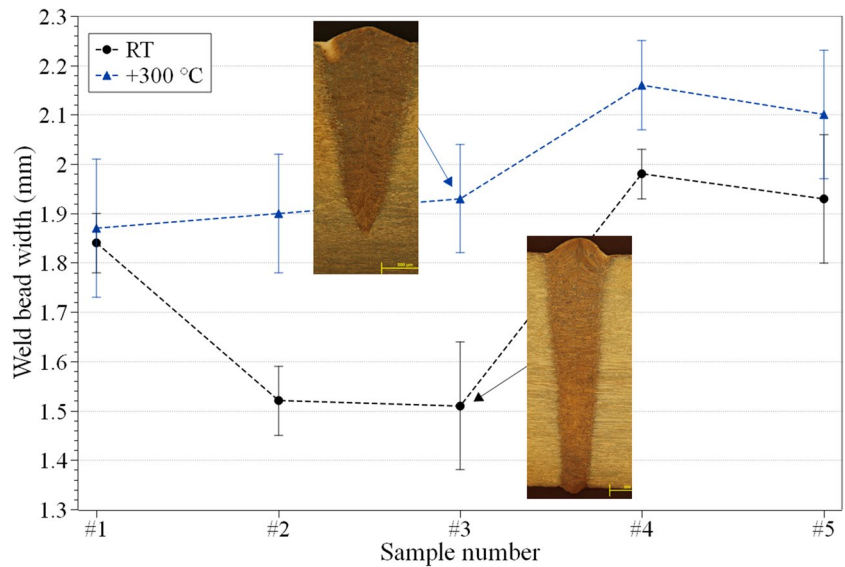
1.84 ± 0.06 mm, 1.98 ± 0.05 mm, and 1.93 ± 0.13 mm. When the laser beam power decreased form 6 kW (#1) to 3.0 and 4.5 kW (#2 and #3, respectively), the weld bead width also decreased to 1.52 ± 0.07 mm and 1.51 ± 0.13 mm, contrary to that the travel speed also changed to keep the heat input constant theoretically. Except sample #1 (6 kW laser beam power, and 0 mm focus point distance), the bead width greatly increased due to preheating. This increase is more pronounced in the case of various welding parameters (samples #2, and #3), and lesser in the case of samples #5 and #6. The largest increase in the weld bead width was measured at sample #3 (highlighted in Fig. 4.), where the 300 °C preheating resulted in + 0.42 ± 0.12 mm width increase.

The comparison of the weld bead depths can be seen in Fig. 5. Reviewing the RT samples, it can be seen both the welding parameters and the preheating temperatures have significant effect on the penetration depth. Among samples #1/RT, #2/RT, and #3/RT the deepest penetration was measured in the middle range (#3 welded with 4.5 kW laser beam power, and 37 mm/s travel speed) among the applied parameters. In this case, penetration depth was 5.60 ± 0.32 mm. The focus point distance also has a notable effect on the penetration depth. The deepest penetration among samples #1, #4, and #5 was measured in case of sample #5/300 (+ 2 mm focus point distance), which is 5.53 ± 0.25 mm. Samples #1/300 and #4/300 showed practically the same penetration depth, which were 4.96 ± 0.27 mm and 5.10 ± 0.26 mm, respectively. The preheating to 300 °C significantly decreased the penetration depth (with the increase of the weld bead width) in all the samples. The most significant decrease was measured between samples #1/RT and #1/300 (− 0.96 ± 0.25 mm, highlighted in Fig. 5), and samples #3/RT and #3/300 (− 0.83 ± 0.23 mm). This observation corresponds to results in the scientific literature. Chen et al.

[45] showed that, the preheating lead to an increase in the weld bead width and the weld cross-section. On one hand, they found that the 200 °C preheating temperature resulted in approximately 10% increase in the weld bead width in the case of Nd:YAG laser welding of GTD-111 nickel–based superalloy. On the other hand, the penetration depth did not increase due to the preheating. For this observation, they gave two possible explanations: the heat input increased (and the cooling rate decreased), and the preheating resulted in more laser beam absorption. Keivanloo et al. [46] also found an increasing weld cross-section are with 200 °C preheating in the case of Nd:YAG laser welding of Inconel 718. Their clarification is based on the difference in temperature distribution around the weld pool due to the preheating.

The comparison of the weld cross-section areas and weld shape factors can be seen in Fig. 6. The shape factor is calculated as the ratio of the bead depth and width. Reviewing the RT samples, it can be seen the focus point distance has much significant effect on the weld cross-section area, than the welding parameters. While the weld of sample #1/RT has a cross-section area of 5.10 ± 0.26 mm^2, it increased at the welds on samples #4/RT and #5/RT to 6.48 ± 0.28 mm^2 and 6.07 ± 0.14 mm^2, respectively. Samples #2/RT (4.79 ± 0.17 mm^2) and #3/RT (5.05 ± 0.23 mm^2) showed moderate change in the cross-section area compared to #1/RT. However, these samples showed much greater sensitivity to the preheating temperature. Samples #1/300, #2/300, and #3/300 showed significantly larger cross-section areas compared to the RT samples. The greatest increase was measured in the case of sample #1, which is + 1.02 ± 0.28 mm^2. On the other hand, samples #4/300 (− 2 mm focus point distance) and #5/300 (+ 2 focus point distance) showed only a negligible increase in the cross-section area, 0.08 ± 0.4 mm^2, and 0.26 ± 0.11

Fig. 5 The weld bead depth of the laser beam–welded samples, welded with different parameters, and different preheating temperatures
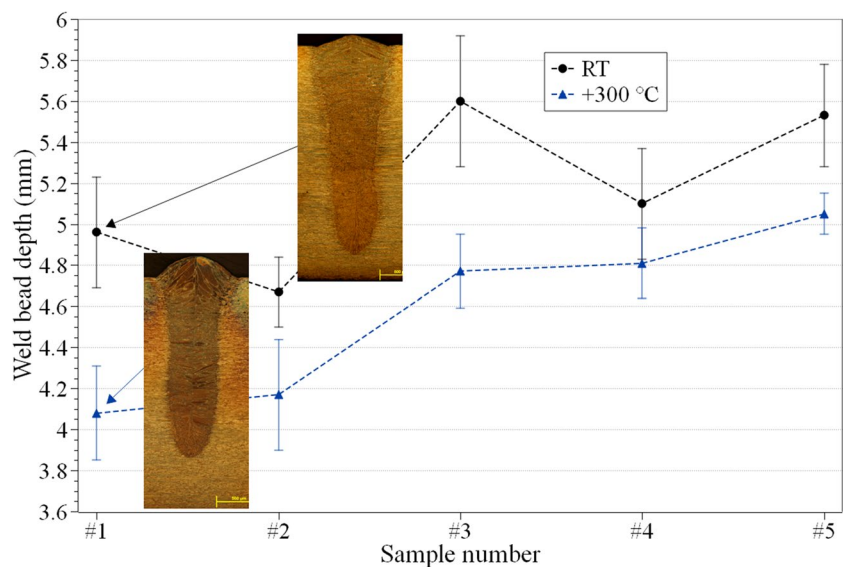
Fig. 6 The weld bead cross-section area and shape factor of the laser beam–welded samples, welded with different parameters and different preheating temperatures
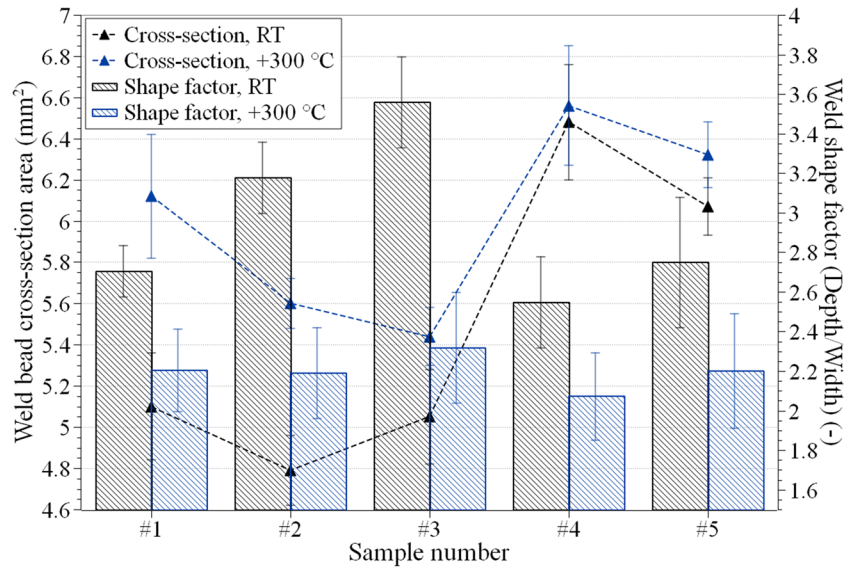

mm^2, respectively. The results of the calculated shape factors also showed important findings. Due to the preheating, the shape factors decreased to a large degree, apart from that the welding parameters of the focus point distances changed. This seems to be a negative effect, as LBW is usually applied because of its high weld shape factors; narrow and deep welds. But, in terms of gap tolerance, it can also be beneficial. The largest decrease in the shape factor was measured at sample #3, from 3.56 ± 0.23 to 2.32 ± 0.28.

3.3 Weld metal microstructure and austenite content

The weld metal and heat affected zone microstructures of all laser beam–welded samples can be seen in Fig. 7. It is known, LBW results is mostly ferritic microstructure both in the WM and in the HAZ. The reason for this is the very low heat input during welding, which results in rapid cooling rates between 1200 and 800 °C, where the ferrite to austenite formation is driven by atomic diffusion in the ferrite phase.

Fig. 7 The microstructure of the weld metal and heat affected zone of the laser beam–welded samples, welded with different parameters, and different preheating temperatures
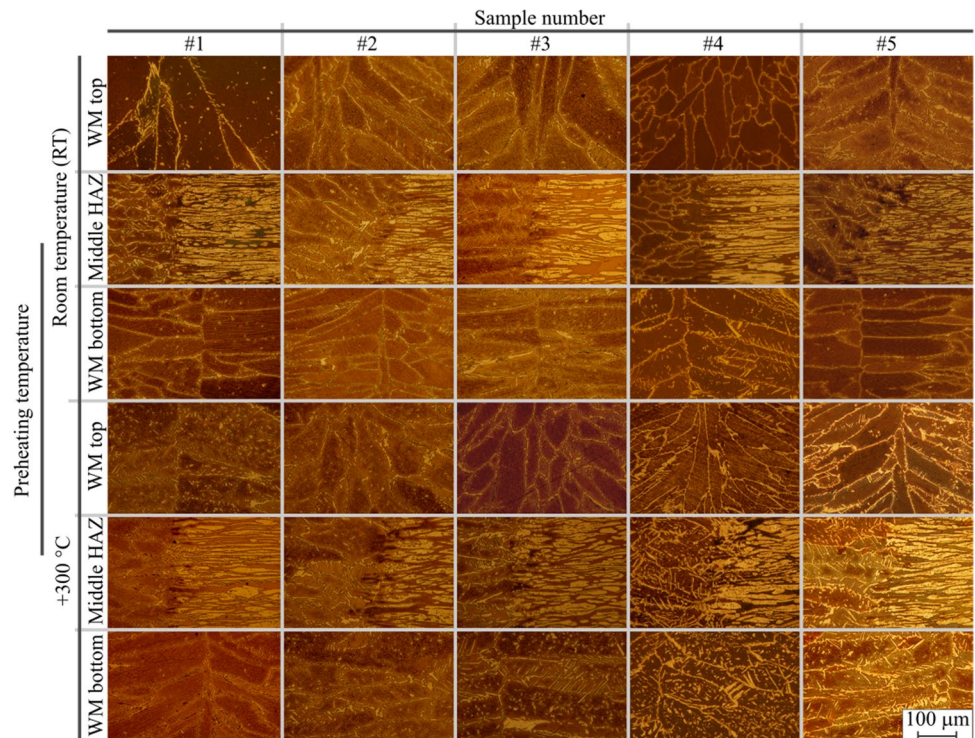
The lack of diffusion time suppresses the solid-state phase transformation, so the microstructure remains predominantly ferritic. This is shown in all the RT samples in Fig. 7, where the used Beraha's etchant tints only the ferrite phase dark. Both the top and bottom parts of the weld showing elongated ferrite grains with grain boundary austenite (GBA) formation. The ferrite grain size did not significantly change at the different welding parameters and focus point distances. At the top part of the welds the average ferrite grain size varied in-between 280 and 410 μm, but extremely large, ~650 μm big ferrite grains were also found in the WM. The reason for the ferrite grain growth is its high grain boundary diffusion at high temperatures. As austenite formation is practically negligible, there is no barrier for grain boundary diffusion, so grain coarsening can be experienced on the contrary to the very high cooling rate. Also, the HAZ showed no significant difference in the microstructure among the RT-welded samples. The HAZ is usually highly ferritic, even in the case of arc welding of DSSs. As the heat input is very low, the HAZ width is also very narrow. Taking an average of all the RT-welded samples, the HAZ width is ~50 μm, but it is very hard to distinguish between the high temperature HAZ and the WM. The bottom part of the RT-welded WM showed the same highly ferritic microstructure with GBA austenite formation. At the bottom side, some intergranular austenite (IGA) formation is also visible inside the ferrite grains as austenitic islands. This formation is more pronounced in the case of samples #1/RT and #4/RT. However, this IGA formation is very dispersed in small sizes (5–10 μm); thus, it does not affect the phase ratio significantly. Also, regarding the GBA formation at the bottom part of the WM, some wider plates austenitic grains are visible, more pronounced in samples #4/RT and #5/RT. Due to the 300 °C preheating, the austenite content visible increased both on the top

and bottom parts of the welds. More IGA formation can be observed, as more time was available for diffusion. Also, this is the reason for visibly wider plates of GBA at the ferrite boundaries. On the top part of the welds, significant differences in the phase balance are visible in the case of the samples #1/300, #4/300, and #5/300. In case of the HAZ microstructure, more IGA formation is obvious at samples #2/300, #4/300, and #5/300. The bottom parts of welds showed even more significant austenite formation, as it can be seen at #/300, #3/00, #4/300, and #5/300. On the other hand, no significant grain coarsening is visible at any of the preheated sample microstructures.

The austenite content of the weld metal of all laser beam–welded samples can be seen in Fig. 8. Reviewing the RT samples, neither the welding parameters nor the focus point distance had a notable effect on the austenite content at the top and bottom parts of the WM. All of the austenite contents remained under 13%, which is detrimental to the toughness and to the corrosion resistance. The bottom part of the WM showed ~2% higher austenite content in most of the cases, except sample #1/RT, where the difference between the top and the bottom parts of the WM in austenite content is $4.9 \pm 1.5\%$. The reason for this is the more pronounced IGA formation in the ferrite grains. The 300 °C preheating increased the austenite content in all cases, as previously expected. It is also visible in Fig. 9. The bottom part of the WM had higher austenite contents again. In the case of the preheated samples, the focus point distance had major influence on the austenite content of the WM. The samples #4/300 and #5/300 showed the highest austenite contents both at the top and at the bottom parts. The highest measured austenite content was $22.1 \pm 2.5\%$ at the bottom part of #5/300, as highlighted in Fig. 8. It was found that the defocus distance (or focus point distance) increased the

Fig. 8 The austenite content of the laser beam–welded samples, welded with different parameters and different preheating temperatures
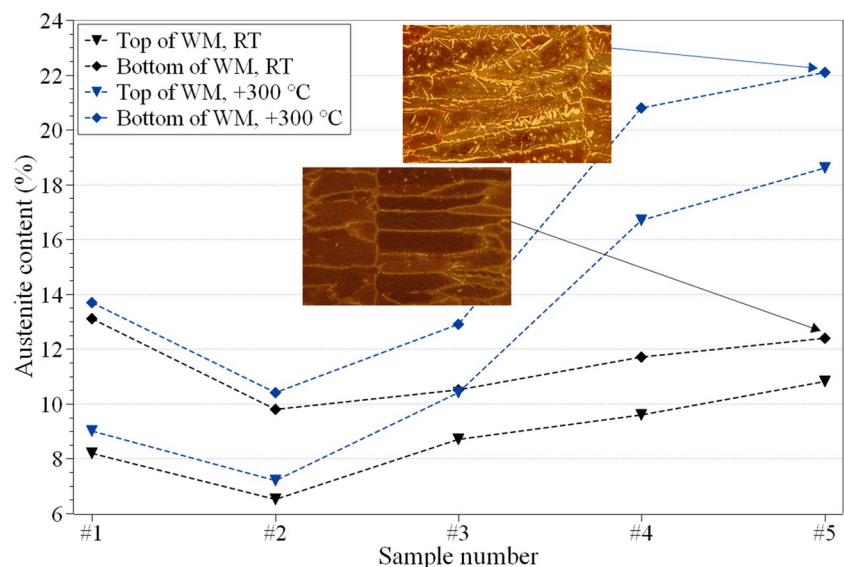
Fig. 9 The potentiodynamic polarization curves of samples #1 and #5 in 3.5% NaCl electrolyte, at room temperature
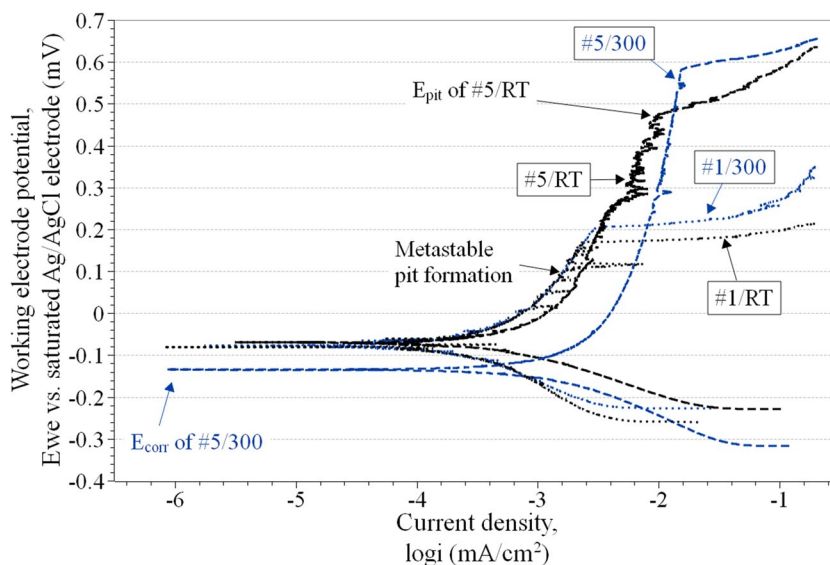
weld bead width and depth, and thus, the weld metal cross-section has also increased. This means that, the actual heat input was higher in the case of samples #4 and #5, comparing to the sample #1, where the welding parameters were the same, except the focus point distance. The higher actual heat input results in slower cooling rate, which promotes the ferrite-to-austenite phase transformation, mainly in the 1200 to 800 °C temperature range. The preheating also resulted in lower cooling rates, which allowed more IGA formation and GBA widening through diffusion. During our microstructure examinations, no signs of intermetallic formation were found in any of the samples.

3.4 Corrosion testing results

From the potentiodynamic polarization curves two important potentials can be described. The corrosion potential (E_{corr}) refers to the passivation behavior of the working electrode. The E_{corr} can be defined as the intersection of the cathodic (reduction) and anodic (oxidation) curves and can be described graphically. The more positive E_{corr} value means more noble behavior. The other important specific point is the pitting potential (E_{pit}). The E_{pit} shows the starting potential of stable pit formation, where the corrosion current density is sharply monotonic increasing. The higher E_{pit} means higher resistance against pitting corrosion. Samples #1 and #5 were selected for performing electrochemical corrosion tests, because during the evaluation of the weld geometry and microstructure, it was confirmed that the focus point distance has a major effect on the welds. The other reason was the high difference in austenite content between samples #1 and #5. In the case of duplex stainless steels, the mechanical and corrosion properties are optimal, when the phase ratio is around the annealed state. The alloying

element distribution in the ferrite and austenite phases and their ratio to each other determines the corrosion resistance, mainly the pitting corrosion resistance in Cl-bearing environments. Thus, the austenite content has a high influence on the pitting corrosion resistance.

The potentiodynamic polarization curves of samples #1/RT, #1/300 and #5/RT, #5/300 in 3.5% NaCl electrolyte at room temperature can be seen in Fig. 9. All of the given working electrode potentials are versus saturated Ag/AgCl reference electrode. Reviewing the RT samples, a difference in the E_{corr} and E_{pit} values can be seen between the samples #1/RT and #5/RT. All of the four polarization curves show the same shape. The quantitative results of the potentiodynamic polarization tests can be seen in Table 3. After the reduction section, oxidation started practically at the same potential level in all cases, for #1/RT it was -80±12 mV, for #5/RT −66±13 mV in average. In the case of sample #1/300 the E_{corr} value did not significantly change to the effect of preheating, the average was measured as −94±11 mV. However, significant improvement was measured for sample #5/300, where the E_{corr} increased to −142±18 mV. This improvement is all originated from the governing microstructures. The scientific literature has previously shown that slower cooling rates result in higher austenite

Table 3 Results of the electrochemical corrosion tests of the laser beam–welded 2120 samples #1 and #5

Sample no	E_{corr} vs. Ag/AgCl (mV)	E_{pit} vs. Ag/AgCl (mV)
#1/RT	− 80 ± 12	170 ± 32
#1/300	− 94 ± 11	210 ± 40
#5/RT	− 66 ± 13	490 ± 38
#5/300	− 142 ± 18	580 ± 39

content, which also means higher pitting potential [47–49] and, thus, higher corrosion resistance. Our research also showed that the higher austenite content (due to the slower cooling rate by the preheating) showed better corrosion resistance. Samples #1/RT, and #5/RT had almost the same austenite contents at the top and bottom parts of the WMs. Some improvement in the austenite content was measured for #1/300, which resulted a slightly higher E_{corr} value compared to #1/RT, but this improvement is practically negligible. On the other hand, preheating had significant effect at #5/300, where the austenite content was measured the highest, $18.6 \pm 1.4\%$ at the top, and $22.1 \pm 2.5\%$ at the bottom part. In the anodic oxidation section, some metastable pit formation is also visible for all of the four measured samples, which appears as sharp but non-monotonic increases in the current density (Fig. 9.). The pitting potentials, where the current density is increasing sharply monotonic, showed larger difference among the samples. Higher pitting potential was measured for #5/RT than #1/RT. Stable pits usually form in the ferrite phase for DSSs, as shown by several researchers, e.g., [47, 48]. The sample #1/RT has lower minimum austenite content ($8.2 \pm 1.5\%$ at the top part of the WM) compared to #5/RT, thus the stable pitting formation starts at lower potentials. The preheating to 300 °C, and the promotion of austenite formation, increased the E_{pit} values in all the examined cases. For sample #1, the preheating increased the E_{pit} values from 170 ± 32 to 210 ± 40 mV. For sample #5, higher increase was measured, from 490 ± 38 to 580 ± 39 mV. Also, the sample #5/300 showed the highest austenite contents both on the top and bottom parts of the WM, which is confirmed by the higher pitting corrosion resistance.

4 Conclusions

In our research, the autogenous fiber laser beam welding of a newly developed NSSC 2120 type lean duplex stainless steel was investigated. For the welding experiments, different welding parameters, focus point distances, and preheating temperatures (room temperature, and $+300$ °C) were used. The welds were evaluated by macroscopic and microstructural investigations, and by electrochemical corrosion tests. From our results, the following conclusions can be drawn:

- Significant differences can be seen in the weld geometry due to the change of welding parameters, focus point distances, and preheating temperatures. Changing the focus point distance resulted in narrower and deeper welds.
- The 300 °C preheating temperature resulted in wider and shallower welds in all cases, with increasing weld cross-section area. The reason for this is the changed temperature gradient around the fusion zone, which resulted lower cooling rates, and different thermal convection circumstances. This can be beneficial in increasing the gap tolerance of laser beam welding.

- All of the examined weld metals had predominantly ferritic microstructure. The preheating temperature (and the lower cooling rate) resulted in higher austenite contents, due to the longer diffusion times, and the presence of intergranular austenite.
- The potentiodynamic polarization tests showed no major difference of the corrosion potential among the investigated samples. However, as the austenite content increased due to the change of focus point distance and applying preheating temperatures, higher pitting potentials (higher pitting corrosion resistance) were measured in all the investigated samples.

Declarations

Competing interests The authors declare no competing interests.

References

1. Francis R, Byrne G (2021) Duplex stainless steels—alloys for the 21st century. Metals (Basel) 11:836. https://doi.org/10.3390/met11050836
2. Pezzato L, Calliari I (2022) Advances in duplex stainless steels. Materials 15:7132. https://doi.org/10.3390/ma15207132

3. Świerczyńska A, Łabanowski J, Michalska J, Fydrych D (2017) Corrosion behavior of hydrogen charged super duplex stainless steel welded joints. Mater Corros 68:1037–1045. https://doi.org/10.1002/maco.201709418

4. Touileb K, Hedhibi AC, Djoudjou R et al (2022) Mechanical, microstructure, and corrosion characterization of dissimilar austenitic 316L and duplex 2205 stainless-steel ATIG welded joints. Materials 15:2470. https://doi.org/10.3390/ma15072470

5. Alfonsson E (2010) Lean duplex—the first decade of service experience. In: Proceedings of the conference duplex stainless steels, Beaune, France, 13–15 October 2010; KCI: Zutphen, The Netherlands

6. Coudreuse L, Ligier V, Audouard JP, Soulignac P (2003) Lean duplex stainless steel for oil and gas applications. In: CORROSION 2003. NACE International, San Diego, CA, pp 16–20

7. Johansson E, Pettersson R (2010) Lean duplex stainless steel within the oil and gas industry. In: European Corrosion Congress ; Gubkin Russian State University of Oil and Gas: Moscow, Russia 4:2869–2878

8. Mészáros I (2011) Magnetic measurement and model based characterisation of phase transformation in lean duplex stainless steel. Mater Sci Forum 721:96–101

9. Pandey C, Thakare JG, Tharaphadar P et al (2021) Characterization of the soft zone in dissimilar welds joint of 2.25Cr-1Mo and lean duplex LDX2101 steel. Fusion Eng Design 163:112147. https://doi.org/10.1016/j.fusengdes.2020.112147

10. Nilsson J-O (2016) The role of nickel and manganese in duplexes. Stainless Steel World 28–29

11. Quiroz V, Gumenyuk A, Rethmeier M (2012) Laser beam weldability of high-manganese austenitic and duplex stainless steel sheets. Welding World 56:9–20. https://doi.org/10.1007/BF03321140

12. Stradomski G, Szarek A, Rydz D (2020) Influence of copper addition on sigma phase precipitation during hot deformation of duplex steel. Materials 13:1665. https://doi.org/10.3390/ma13071665

13. Westin EM, Johansson MM, Pettersson RFA (2013) Effect of nitrogen-containing shielding and backing gas on the pitting corrosion resistance of welded lean duplex stainless steel LDX 2101® (EN 1.4162, UNS S32101). Welding World 57:467–476. https://doi.org/10.1007/s40194-013-0046-2

14. Mészáros I (2013) Thermal induced phase transformations in duplex stainless steel. Mater Sci Forum 729:109–113

15. Padilha AF, Aguiar DJM, Plaut RL (2012) Duplex stainless steels: a dozen of significant phase transformations. Defect and Diffusion Forum 322:163–174. https://doi.org/10.4028/www.scientific.net/DDF.322.163

16. Berecz T, Szabó PJ (2005) Study of the isothermal phase transformations in duplex stainless steels by EBSD method. Mater Sci Forum 473(474):177–182

17. Ogawa K (2022) Austenite phase growth behaviour in continuous cooling from high temperature in duplex stainless steel. ISIJ International 62:ISIJINT-2021–376. https://doi.org/10.2355/isijinternational.ISIJINT-2021-376

18. Mohan DG, Tomków J, Karganroudi SS (2022) Laser welding of UNS S33207 hyper-duplex stainless steel to 6061 aluminum alloy using high entropy alloy as a filler material. Appl Sci (Switzerland) 12:2849. https://doi.org/10.3390/app12062849

19. Payares-Asprino C (2021) Prediction of mechanical properties as a function of welding variables in robotic gas metal arc welding of duplex stainless steels SAF 2205 welds through artificial neural networks. Adv Mater Sci 21:75–90. https://doi.org/10.2478/adms-2021-0019

20. Shen K, Jiang W, Sun C et al (2022) Unlocking the influence of microstructural evolution on hardness and pitting corrosion in duplex stainless welded joints. Corros Sci 206:110532. https://doi.org/10.1016/j.corsci.2022.110532

21. Ogawa K, Yamada K, Seki A (2022) Modelling of nitride precipitation during isothermal heating after rapidly cooled from high temperature in duplex stainless steel. ISIJ International 62:ISIJINT-2022–113. https://doi.org/10.2355/isijinternational.ISIJINT-2022-113

22. Yoon B-J, Ahn Y-S (2022) Effect of aging on pitting corrosion resistance of 21Cr lean duplex stainless steel with different molybdenum contents. J Mater Eng Perform. https://doi.org/10.1007/s11665-022-07478-w

23. Wang L, Zhao P, Pan J et al (2021) Investigation on microstructure and mechanical properties of double-sided synchronous TIP TIG arc butt welded duplex stainless steel. Int J Adv Manuf Technol 112:303–312. https://doi.org/10.1007/s00170-020-06375-7

24. Fábián ER, Dobránszky J, Csizmazia J, Ott R (2017) Effect of laser beam welding on the microstructure of duplex stainless steels. Mater Sci Forum 885:245–250. https://doi.org/10.4028/www.scientific.net/MSF.885.245

25. Landowski M (2019) Influence of parameters of laser beam welding on structure of 2205 duplex stainless steel. Adv Mater Sci 19:21–31. https://doi.org/10.2478/adms-2019-0002

26. Odermatt AE, Ventzke V, Dorn F et al (2021) Effect of laser beam welding on microstructure, tensile strength and fatigue behaviour of duplex stainless steel 2205. J Manuf Process 72:148–158. https://doi.org/10.1016/j.jmapro.2021.10.020

27. Tóth T, Krasnorutskyi S, Hensel J, Dilger K (2021) Electron beam welding of 2205 duplex stainless steel using pre-placed nickel-based filler material. Int J Press Vessels Pip 191:104354. https://doi.org/10.1016/j.ijpvp.2021.104354

28. Maurya AK, Pandey SM, Chhibber R, Pandey C (2023) Structure–property relationships and corrosion behavior of laser-welded X-70/UNS S32750 dissimilar joint. Arch Civil Mech Eng 23:81. https://doi.org/10.1007/s43452-023-00627-5

29. Gou N-N, Zhang J-X, Zhang L-J et al (2016) Single pass fiber laser butt welding of explosively welded 2205/X65 bimetallic sheets and study on the properties of the welded joint. Int J Adv Manuf Technol 86:2539–2549. https://doi.org/10.1007/s00170-015-8335-0

30. Tóth T, Hensel J, Hesse A-C, Dilger K (2022) Electron beam welding of 2205 duplex stainless steel with nickel-based filler wire using multi-beam technique. Welding World 66:2191–2206. https://doi.org/10.1007/s40194-022-01363-9

31. Westin EM, Brolund B, Hertzman S (2008) Weldability aspects of a newly developed duplex stainless steel LDX 2101. Steel Res Int 79:473–481

32. Keskitalo M, Mäntyjärvi K, Sundqvist J et al (2015) Laser welding of duplex stainless steel with nitrogen as shielding gas. J Mater Process Technol 216:381–384. https://doi.org/10.1016/j.jmatprotec.2014.10.004

33. Lai R, Cai Y, Wu Y et al (2016) Influence of absorbed nitrogen on microstructure and corrosion resistance of 2205 duplex stainless steel joint processed by fiber laser welding. J Mater Process Technol 231:397–405. https://doi.org/10.1016/j.jmatprotec.2016.01.016

34. Zhang X-Y, Zha X-Q, Gao L-Q et al (2021) Influence of shielding gas on microstructure and properties of GMAW DSS2205 welded joints. Materials 14:2671. https://doi.org/10.3390/ma14102671

35. Schmigalla S, Krasnorutskyi S, Zinke M, Heyn A (2015) Corrosion behavior of electron beam welded duplex stainless steels. Mater Corros 66:442–452. https://doi.org/10.1002/maco.201307483

36. Krasnorutskyi S, Keil D, Schmigalla S et al (2012) Metallurgical investigations on electron beam welded duplex stainless steels.

Welding in the World 56:34–40. https://doi.org/10.1007/BF033 21393

37. KoleniČ F, Kovac L, Drimal D (2011) Effect of laser welding conditions on austenite/ferrite ratio in duplex stainless steel 2507 welds. Welding in the World 55:19–25. https://doi.org/10.1007/BF03321292

38. Saravanan S, Raghukandan K, Sivagurumanikandan N (2017) Pulsed Nd: YAG laser welding and subsequent post-weld heat treatment on super duplex stainless steel. J Manuf Process 25:284–289. https://doi.org/10.1016/j.jmapro.2016.12.015

39. Köse C, Topal C (2022) Texture, microstructure and mechanical properties of laser beam welded AISI 2507 super duplex stainless steel. Mater Chem Phys 289:126490. https://doi.org/10.1016/j.matchemphys.2022.126490

40. Oikawa Y, Tsuge S, Gohnome F (2021) Development of new lean duplex stainless steel series NSSC 2120[TM], NSSC[TM] 2351. Nippon steel technical report No. 126

41. Varbai B, Májlinger K (2019) Optimal etching sequence for austenite to ferrite ratio evaluation of two lean duplex stainless steel weldments. Measurement 147:106832. https://doi.org/10.1016/j.measurement.2019.07.060

42. Havrilla D (1999) Process fundamentals of industrial laser welding and cutting. Rofin-Sinar, Inc., Plymouth

43. Guo SH, Zou JL, Xiao RS (2020) Characterizations of welding mode transformation process during 1-μm and 10-μm laser welding. AIP Adv 10. https://doi.org/10.1063/1.5132776

44. Su J, Qiu X, Xing F, Ruan Y (2019) Effect of preheating temperature on microstructure and properties of 42CrMo4/38MnVS6 heterogeneous laser welded joint. Metals (Basel) 9:870. https://doi.org/10.3390/met9080870

45. Chen Z, Taheri M (2020) The effect of pre-heating and pre-cold treatment on the formation of liquation and solidification cracks of nickel-based superalloy welded by laser beam. J Market Res 9:11162–11177. https://doi.org/10.1016/j.jmrt.2020.07.053

46. Keivanloo A, Naffakh-Moosavy H, Miresmaeili R (2021) The effect of pulsed laser welding on hot cracking susceptible region size and weld pool internal geometry of Inconel 718: Numerical and experimental approaches. CIRP J Manuf Sci Technol 35:787–794. https://doi.org/10.1016/j.cirpj.2021.09.001

47. Zhang L, Zhang W, Jiang Y et al (2009) Influence of annealing treatment on the corrosion resistance of lean duplex stainless steel 2101. Electrochim Acta 54:5387–5392. https://doi.org/10.1016/j.electacta.2009.04.023

48. Pezzato L, Lago M, Brunelli K et al (2018) Effect of the heat treatment on the corrosion resistance of duplex stainless steels. J Mater Eng Perform 27:3859–3868. https://doi.org/10.1007/s11665-018-3408-5